Article | Open Access

Energy Materials

Huang *et al. Energy Mater.* **2026**, *6*, 600154 **DOI:**10.20517/energymater.2026.269

Interfacial coordination reconstruction via electrochemical phase transformation for stable zinc powder anodes

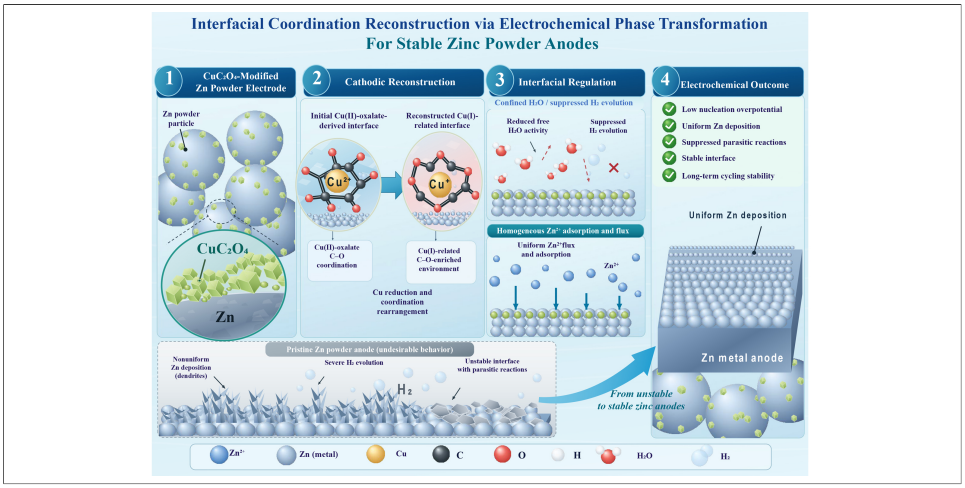
Can Huang[1,#], Yuan Li[2,#], Penghui Cao[1,3,4,*], Xinqi Yang[1], Shimin Yao[1], Huali Zhu[1], Juan Yang[5], Chuanchang Li[1,3,4], Xiongjun Liu[2,*], Zhaoping Lu[2,*]

Keywords:
Zinc powder anode, interface, phase transformation, coordination reconstruction

Citation: Huang, C.; Li, Y.; Cao, P.; Yang, X.; Yao, S.; Zhu, H.; Yang, J.; Li, C.; Liu, X.; Lu, Z. Interfacial coordination reconstruction via electrochemical phase transformation for stable zinc powder anodes. *Energy Mater.* **2026**, *6*, 600154. https://dx.doi.org/10.20517/energymater.2026.269

Received: 12 Aug 2026
First Decision: 4 Sep 2026
Revised: 29 Sep 2026
Accepted: 14 Oct 2026
Published: 13 Nov 2026

Academic Editor: Yuping Wu
Copy Editor: Ping Zhang
Production Editor: Ping Zhang



Abstract

The practical development of aqueous zinc-ion batteries is hampered by the intrinsic thermodynamic instability of zinc powder anodes, where uncontrolled parasitic reactions and dendritic growth lead to rapid capacity decay. Conventional interfacial protection layers, whether pre-fabricated or *in-situ* formed, suffer from mechanical and chemical degradation under dynamic cycling conditions. Here, we report an interface regulation strategy based on an electrochemically driven phase transformation of copper oxalate (CuC_2O_4) embedded in the zinc powder electrode. Upon discharge, the CuC_2O_4 undergoes a structural reconstruction involving the conversion of C=O to C-O coordination environments and the partial reduction of Cu^{2+} to Cu^{+}, as evidenced by multi-modal

[1]Key Laboratory of Renewable Energy Electric-Technology of Hunan Province, College of Energy and Power Engineering, Changsha University of Science and Technology, Changsha 410114, Hunan, China.
[2]State Key Laboratory for Advanced Metals and Materials, University of Science and Technology Beijing, Beijing 100083, China.
[3]State Key Laboratory of Disaster Prevention & Reduction for Power Grid, Changsha University of Science & Technology, Changsha 410114, Hunan, China.
[4]Turpan Solar Thermal Resource Development and Utilization Expert Workstation, Changsha University of Science and Technology, Turpan 838000, Xinjiang, China.
[5]School of Metallurgy and Environment, Central South University, Changsha 410083, Hunan, China.
[#]These authors contributed equally to this work.

[*]**Correspondence to:** Prof. Penghui Cao, Key Laboratory of Renewable Energy Electric-Technology of Hunan Province, College of Energy and Power Engineering, Changsha University of Science and Technology, Changsha 410114, Hunan, China; State Key Laboratory of Disaster Prevention & Reduction for Power Grid, Changsha University of Science & Technology, Changsha 410114, Hunan, China; Turpan Solar Thermal Resource Development and Utilization Expert Workstation, Changsha University of Science and Technology, Turpan

838000, Xinjiang, China. E-mail: CaoPH@csust.edu.cn; Prof. Xiongjun Liu, Prof. Zhaoping Lu, State Key Laboratory for Advanced Metals and Materials, University of Science and Technology Beijing, Beijing 100083, China. E-mail: xjliu@ustb.edu.cn; luzp@ustb.edu.cn

spectroscopy and X-ray photoelectron spectroscopy. This reconstructed interface, enriched with C-O groups and Cu^+ sites, exhibits enhanced zinc affinity and water confinement, as quantified by density functional theory calculations, thereby suppressing parasitic hydrogen evolution and guiding uniform zinc deposition. As a result, the modified zinc powder anode (ZP@CuC_2O_4) delivers a stable cycling lifetime of approximately 600 h under high-rate conditions (7 mA cm^{-2}/1 mAh cm^{-2}) in symmetric cells and enables pouch-type full cells to deliver a cumulative capacity of 11.7 Ah after 1,000 cycles at 7 A g^{-1}. This work demonstrates a paradigm of dynamic interfacial engineering through intrinsic phase-transition-induced coordination reconstruction, addressing a key barrier for practical zinc powder anodes.

INTRODUCTION

Rechargeable aqueous zinc-ion batteries (AZIBs) are regarded as a promising large-scale energy storage technology due to their inherent safety, cost-effectiveness, and environmental friendliness[1-4]. However, their practical application is largely limited by the interfacial instability of the zinc anode[5,6]. Compared to zinc foil, which is commonly used in basic research, zinc powder anodes offer a higher specific surface area and are favored by industry for scalable electrode fabrication[7]. Yet, this high surface area exacerbates parasitic reactions such as hydrogen evolution and corrosion during cycling. Moreover, the substantial volume changes of zinc particles easily lead to fragmentation, loss of electrical contact, accumulation of "dead zinc", and rapid coulombic efficiency decay[8-11]. Therefore, stabilizing the interface of zinc powder anodes has become a critical challenge for the commercialization of AZIBs.

The failure of zinc powder anodes essentially stems from uncontrolled ion transport and deposition behavior at the electrode-electrolyte interface[12,13]. An ideal interface layer should not merely serve as a physical barrier but should actively regulate Zn^{2+} flux and deposition kinetics. Various strategies have been explored, including the construction of conductive frameworks, crystal orientation regulation[14-16], and electrolyte engineering[17,18]. However, most of them rely on prefabricated static structures. Such "pre-set" protective layers often fail in dynamically evolving local environments during electrochemical cycling, particularly under severe volume fluctuations at high areal capacity. Cracking, delamination, and eventual loss of protection are common.

In response to these limitations, recent efforts have focused on *in situ* formation of stable interfacial phases[19,20]. Although *in situ*-formed solid electrolyte interphase (SEI)-like films can passivate the surface to some extent, maintaining stable and effective interfacial regulation over extended cycling remains challenging[21-23]. The key scientific challenge is thus overcoming the "rigidity" of the interfacial chemistry to shift from "passive protection" to "active regulation" that evolves synergistically with electrochemical processes.

Here, we propose an interface regulation strategy based on copper oxalate (CuC_2O_4) embedded directly into the zinc powder electrode matrix, rather than being introduced as an electrolyte additive. Unlike conventional *in situ* SEI formation[19,20], CuC_2O_4 is not a static coating but a functional component that undergoes a discharge-triggered phase transition. The phase transformation refers to the electrochemically driven conversion of crystalline Cu(II)-oxalate into a structurally disordered, C-O-enriched and Cu^+-containing interphase, rather than a conventional crystallographic phase transition between two well-defined crystalline phases. During cathodic polarization, the Cu(II)-oxalate framework becomes destabilized in the hydrated electrochemical environment, leading to a coupled evolution of the carbon-oxygen coordination

environment (from C=O-rich to C-O-enriched) and reduction of Cu^{2+} to Cu^{+}. Consequently, the interface dynamically reconstructs into a new phase rich in C-O groups and Cu^{+}-related active sites, which modulates Zn^{2+} adsorption/desolvation and suppresses competitive water reduction. As a result, the CuC_2O_4-modified zinc powder anode (ZP@CuC_2O_4) exhibits significantly enhanced cycling stability. In Zn||Zn symmetric cells, it operates stably for approximately 600 h at 7 mA cm^{-2}/1 mAh cm^{-2} and shows a substantial lifespan extension over unmodified controls at 10 mA cm^{-2}/1 mAh cm^{-2}. In Zn||V_2O_5 full cells, ZP@CuC_2O_4 retains a capacity of 78 mAh g^{-1} after 3,600 cycles at 10 A g^{-1} at 25 °C. At 40 °C, it maintains approximately 118 mAh g^{-1} after 800 cycles at 10 A g^{-1}. Moreover, pouch-type full cells deliver a cumulative capacity of 11.7 Ah after 1,000 cycles at 7 A g^{-1}. This work demonstrates that intrinsic, phase-transition-driven interfacial coordination reconstruction can transform a zinc powder anode from a passively protected electrode to an actively regulating system, offering a new paradigm for durable aqueous zinc batteries.

EXPERIMENTAL

Preparation of zinc anode

To prepare the zinc powder electrode (ZP), flake-like zinc powder and polyvinylidene fluoride (PVDF) binder were mixed at a weight ratio of 98:2, with a total mass of 1 g. The powders were first ground uniformly in an agate mortar, and then N-methyl-2-pyrrolidone (NMP) was added to obtain a homogeneous slurry. The resulting slurry was coated onto copper foil using a doctor blade with a thickness of 100 μm and dried overnight at 55 °C under vacuum to yield the ZP electrode. For the preparation of the copper oxalate-modified zinc powder electrode (ZP@CuC_2O_4), zinc powder, copper oxalate, and PVDF were mixed at a mass ratio of 96:2:2, with a total mass of 0.6 g. After thorough dispersion in NMP, the slurry was cast onto copper foil with a 100 μm doctor blade and then dried overnight in a vacuum oven at 55 °C to obtain the final ZP@CuC_2O_4 electrode. For comparison, ZP@CuC_2O_4 electrodes containing 1%, 5%, and 8% copper oxalate were also prepared using the same procedure.

Preparation of electrolytes

The 2 mol L^{-1} $ZnSO_4$ electrolyte was prepared by dissolving 5.7512 g of $ZnSO_4 \cdot 7H_2O$ in deionized water and then diluting the solution to a final volume of 10 mL under continuous stirring until complete dissolution was achieved. For the electrolyte used in full-cell tests, 5.7512 g of $ZnSO_4 \cdot 7H_2O$ and 264 mg of ammonium sulfate [$(NH_4)_2SO_4$] were accurately weighed and mixed. Deionized water was added dropwise during stirring until the total volume reached 10 mL, resulting in a uniform electrolyte solution.

Synthesis of cathode

V_2O_5 was synthesized by a one-step calcination route. Briefly, 1 g of NH_4VO_3 was calcined at 573 K in an argon atmosphere with a heating rate of 5 K min^{-1} and maintained for 2 h. After calcination, the obtained black powder was collected as V_2O_5.

Full battery preparation

The cathode was prepared from V_2O_5 (~0.35 g), Super P, and PVDF at a mass ratio of 7:2:1. These components were mixed in a mortar and ground for 20 min, followed by the addition of 250 μL NMP, after which the mixture was further ground for 15 min to form a uniform slurry. Stainless steel meshes (500 mesh) were used as the current collectors. The meshes were cut into circular pieces with a radius of 5 mm, ultrasonically cleaned in ethanol, and dried in an oven at 50 °C. The prepared cathode slurry was then coated onto the stainless steel meshes, pre-dried at 50 °C for 60 min, and subsequently transferred to a vacuum oven at 60 °C for 12 h. The active-material loading of the cathode for coin cells was about 2.0-3.0 mg cm^{-2}.

Measurements of electrochemical performance

The electrochemical performance of Zn//Zn symmetric cells, Zn//Cu half cells, and Zn//V_2O_5 full cells was evaluated using CR2025 coin cells assembled under ambient conditions. A Whatman Grade GF/D glass microfiber filter was used as the separator, and 2 mol L^{-1} $ZnSO_4$ served as the electrolyte unless otherwise stated. Cyclic voltammetry (CV) measurements were carried out at a scan rate of 0.1 mV s^{-1}. Tafel polarization tests were recorded at 50 mV s^{-1}, and linear sweep voltammetry (LSV) was performed at 10 mV s^{-1}. These electrochemical measurements were conducted on an electrochemical workstation. Galvanostatic cycling tests, including symmetric-cell cycling, full-cell cycling, Coulombic efficiency tests, and overpotential measurements, were performed on a battery testing system (NEWARE MIHW-200-160CH-B, China).

Materials characterization

The surface morphology of the electrodes was examined using a ZEISS Sigma 360 scanning electron microscope (SEM), and the corresponding energy-dispersive X-ray spectroscopy (EDS) elemental mappings were collected on the same instrument. X-ray diffraction (XRD) measurements were conducted on a Rigaku SmartLab SE diffractometer to analyze the crystalline phases on the Zn anode surface. Fourier-transform infrared (FT-IR) spectra were recorded on a Thermo Scientific Nicolet iS50 spectrometer (USA) to identify functional groups and monitor bonding changes. X-ray photoelectron spectroscopy (XPS) was performed using an ESCALAB Xi+ system (Thermo Scientific, USA) to determine the surface chemical composition and valence states. Raman spectra were acquired with a WITec alpha300R spectrometer (Germany).

Post-treatment of cycled electrodes

After electrochemical testing, the cells were disassembled, and the electrodes were gently rinsed with ethanol, followed by vacuum drying at 55 °C for 960 min. The dried electrodes were then transferred under ambient conditions without air-protected transfer for *ex-situ* XRD, XPS, FT-IR, Raman, SEM, and EDS characterizations.

Theoretical calculations

To evaluate the interfacial adsorption behavior of different active sites in the copper oxalate-modified zinc powder electrode, theoretical calculations were carried out to compare the interactions of Zn^{2+} and H_2O with different copper-related surfaces and oxygen-containing coordination environments. Here, the Zn^{2+} adsorbate refers to a desolvated Zn^{2+} species rather than a fully hydrated $[Zn(H_2O)x]^{2+}$ complex. The coordinated hydration shell was not explicitly included in the adsorption models. Therefore, the calculated Zn^{2+} adsorption energies describe the interfacial affinity of desolvated Zn^{2+} toward different surface/coordination sites. The calculations considered two categories of surface models: (1) different copper valence-state-related surfaces, including Zn(001), Cu(111), Cu_2O(111), and CuO(111), corresponding to the intrinsic zinc surface and Cu^0, Cu^+, and Cu^{2+} environments, respectively, and (2) different oxygen coordination sites, including C=O and C-O configurations derived from the copper oxalate-related interfacial environment. For the C=O and C-O models, five initial adsorption configurations were built for each site to account for the influence of different approaching directions of the adsorbates. The adsorption energies of Zn^{2+} and H_2O were calculated to assess zincophilicity, hydrogen interaction, and the affinity of the interface toward water molecules under different coordination environments. The average adsorption energy, energy spread (ΔE), and standard deviation (SD) were further used to evaluate the distribution characteristics of the multi-configuration adsorption energies. More negative adsorption energies indicate stronger interfacial interaction, whereas smaller ΔE and SD values suggest a more uniform adsorption-energy landscape.

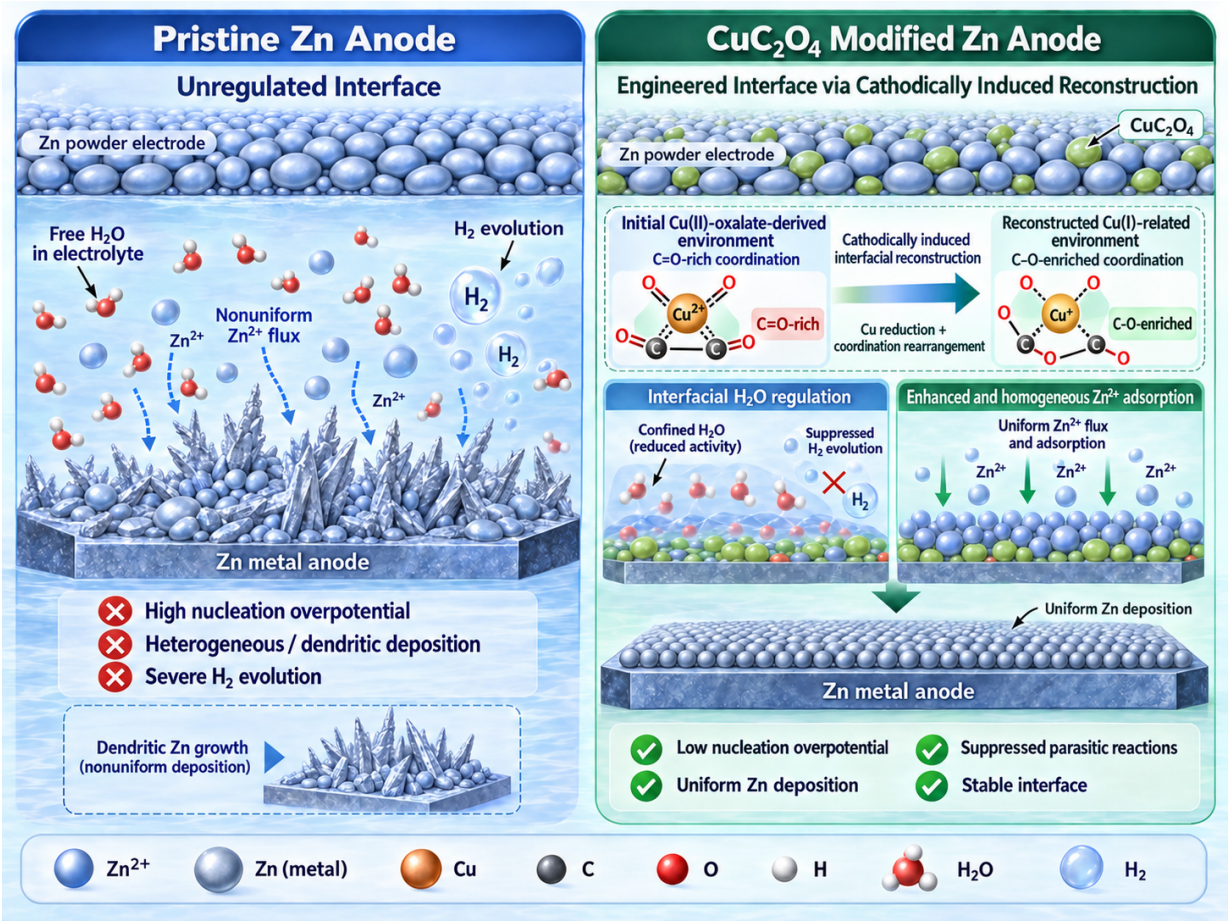


Figure 1. Schematic illustration of copper oxalate-induced interfacial regulation on a zinc powder anode.

RESULTS AND DISCUSSION

Figure 1 schematically illustrates the proposed interfacial regulation mechanism based on CuC_2O_4. In the pristine zinc powder electrode, the particle-packed structure creates spatially dispersed active sites and pronounced local polarization, leading to preferential Zn^{2+} desolvation and nucleation at limited sites, which causes high nucleation overpotential, dendritic growth, and hydrogen evolution[24-27]. In contrast, CuC_2O_4 does not act as a static coating. Instead, it is proposed to undergo a discharge-induced structural and coordination reconstruction at the electrode/electrolyte interface. During cathodic polarization, the original Cu(II)-oxalate units gradually destabilize and evolve toward Cu(I)-related species, while the local carbon-oxygen coordination environment shifts from a C=O-rich state to a more C-O-enriched configuration[28]. This phase transition is attributed to continuous electron injection combined with the interfacial instability of the initial Cu(II)-oxalate framework in the hydrated electrochemical environment, inducing coupled Cu-valence reduction and ligand bonding reorganization. This interpretation is consistent with prior reports on electron-induced oxalate removal/decomposition from Cu(II) oxalate and the conversion-type phase evolution of transition-metal oxalates under electrochemical reduction[28-30]. The resulting interfacial coordination reconstruction generates more uniformly distributed Zn-O interaction sites, enhances local zincophilicity, and simultaneously modulates the interfacial behavior of Zn^{2+} and H_2O. Consequently, Zn^{2+} adsorption and desolvation become more spatially homogeneous, interfacial energy fluctuation and polarization accumulation are alleviated, and the interface selectivity for Zn deposition over parasitic reactions is improved[31,32]. As a result, zinc deposition becomes more uniform and reversible, with suppressed dendritic growth and hydrogen evolution.

To identify the appropriate CuC_2O_4 loading, electrodes containing 1, 2, 5, and 8 wt% CuC_2O_4 were first evaluated in Zn//Zn symmetric cells under different current densities and areal capacities. As shown in Supplementary Figures 1-3 [Supplementary Materials], the electrode containing 2 wt% CuC_2O_4 consistently exhibited the longest lifetime under 0.5 mA cm^{-2}/0.25 mAh cm^{-2}, 5 mA cm^{-2}/1 mAh cm^{-2}, and 7 mA cm^{-2}/1 mAh cm^{-2}. These results indicate that an appropriate CuC_2O_4 content is important for optimizing the electrochemical performance of the Zn powder electrode. The inferior cycling performance at lower CuC_2O_4 contents may reflect insufficient interfacial regulation, whereas the deterioration at higher contents could qualitatively arise from an increased inactive fraction and potentially less favorable electronic/ionic transport within the electrode. However, because systematic impedance or conductivity measurements were not performed for electrodes with different CuC_2O_4 loadings, the latter interpretation remains a qualitative conjecture rather than a quantitatively verified mechanism. Based on the cycling-performance optimization, 2 wt% CuC_2O_4 was therefore selected for subsequent mechanistic and electrochemical investigations, and the corresponding electrode was designated as ZP@CuC_2O_4.

The optimized ZP@CuC_2O_4 electrode exhibits significantly enhanced rate capability and cycling durability compared to the pristine ZP electrode. Under increasing current densities, ZP@CuC_2O_4 maintains reduced voltage hysteresis and stable plating/stripping behavior [Figure 2A]. Specifically, the cycle life extends from 160 h to 650 h at 0.5 mA cm^{-2} [Supplementary Figure 4, Supplementary Materials] and from 192 h to 700 h at 1 mA cm^{-2} /1 mAh cm^{-2} [Figure 2B]. Robust stability is further demonstrated at higher current densities, with stable cycling achieved for 520 h at 5 mA cm^{-2} [Supplementary Figure 5, Supplementary Materials], approximately 600 h at 7 mA cm^{-2}/1 mAh cm^{-2} [Figure 2C], and approximately 370 h under the rigorous condition of 10 mA cm^{-2}/1 mAh cm^{-2}, where the control electrode failed prematurely [Figure 2D]. High zinc utilization and lean-Zn operation are important considerations for evaluating the practical viability of Zn-metal batteries[33]. To further evaluate the deep-discharge tolerance of the Zn powder anode, the areal capacity was increased to 2 mAh cm^{-2} at 7 mA cm^{-2}. Under this more demanding condition, ZP@CuC_2O_4 maintained a more stable voltage response with suppressed polarization growth compared with pristine ZP during repeated Zn plating/stripping [Supplementary Figure 6, Supplementary Materials]. Moreover, the interfacial regulation strategy proves effective at elevated temperatures. At 40 °C, ZP@CuC_2O_4 delivers a stable voltage profile, in contrast to the rapid deterioration of the bare electrode [Figure 2E]. The superior performance of this strategy is highlighted in comparison with previously reported zinc-based electrodes [Figure 2F and Supplementary Table 1, Supplementary Materials]. Consistent trends were observed in Zn//Cu cells. At 0.2 mA cm^{-2}/0.1 mAh cm^{-2}, ZP@CuC_2O_4 sustained 575 cycles with an average coulombic efficiency (CE) of 98.1%, whereas the ZP electrode failed after 187 cycles [Figure 2G]. At 1 mA cm^{-2}/0.5 mAh cm^{-2}, the pristine electrode failed after only 166 cycles with an average CE of 98.63%, while ZP@CuC_2O_4 maintained a high CE of 99.55% for more than 420 cycles [Figure 2H]. These results demonstrate that CuC_2O_4 substantially enhances the reversibility and long-term electrochemical stability of the zinc powder anode.

Electrochemical kinetics and interfacial stability were further examined to clarify how CuC_2O_4 improves the zinc powder anode. The Tafel plots show that ZP@CuC_2O_4 exhibits a lower corrosion current and a more positive corrosion potential than the pristine ZP electrode [Figure 3A], indicating improved corrosion resistance[34]. This protective effect is further corroborated by LSV [Figure 3B], where the ZP@CuC_2O_4 electrode exhibits a reduced cathodic current in the negative potential region compared with the pristine ZP electrode, indicating a suppressed hydrogen evolution reaction[35]. Regarding the deposition kinetics, the nucleation overpotential in Zn//Cu cells decreases from 21.7 to 17.3 mV upon modification [Figure 3C]. This reduction indicates that the CuC_2O_4 modification lowers the Gibbs free energy barrier for zinc nucleation, thereby promoting homogeneous nucleation and mitigating dendrite growth[31,32]. *In situ* electrochemical impedance spectroscopy coupled with distribution of relaxation times (DRT) analysis was employed to

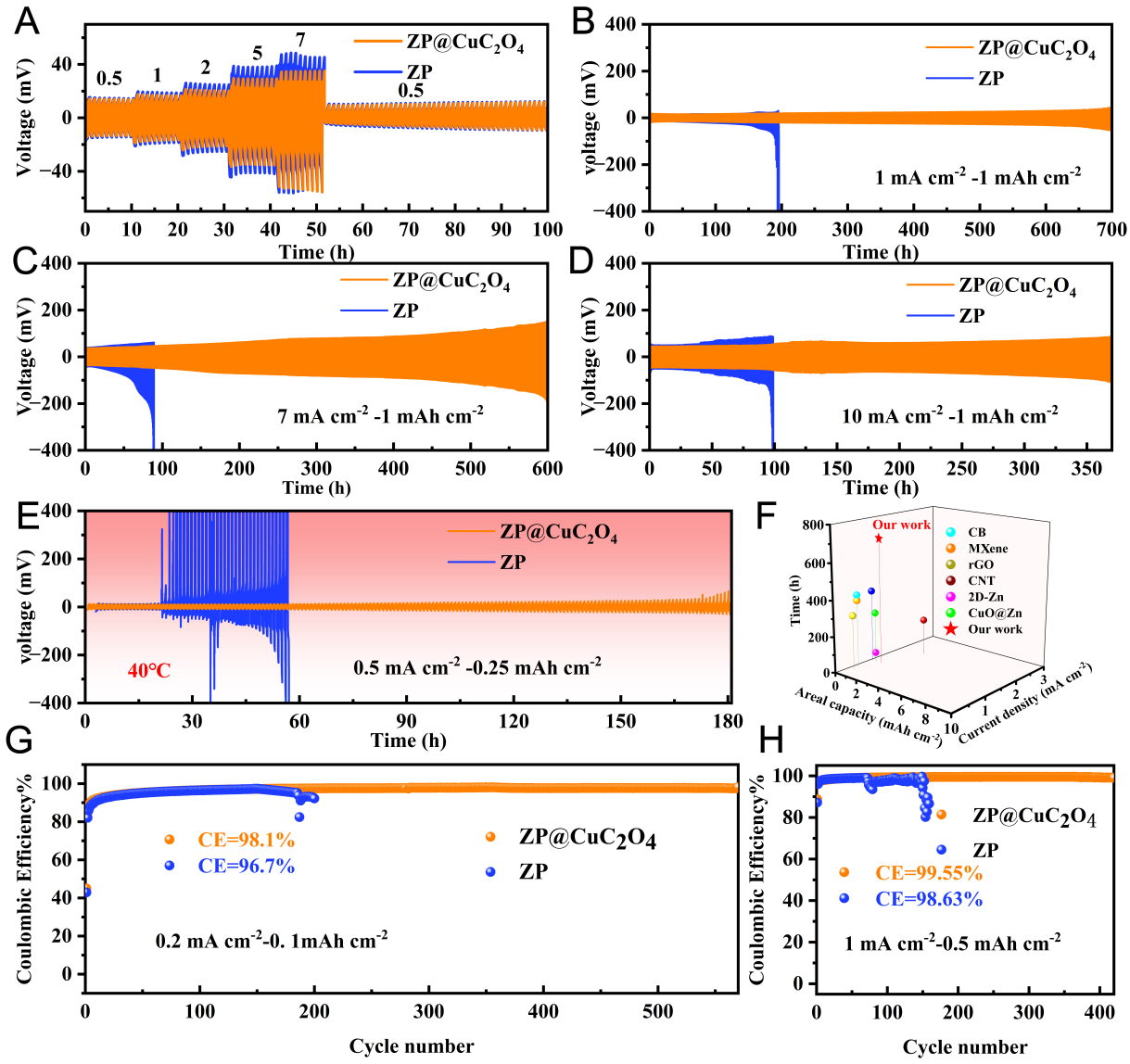


Figure 2. Electrochemical performance of ZP and ZP@CuC_2O_4 electrodes. (A) Rate performance of Zn//Zn symmetric cells under stepwise current-density variation; (B) Galvanostatic cycling of Zn//Zn symmetric cells at 1 mA cm^{-2}/1 mAh cm^{-2} at room temperature; (C) Galvanostatic cycling of Zn//Zn symmetric cells at 7 mA cm^{-2}/1 mAh cm^{-2} at room temperature; (D) Galvanostatic cycling of Zn//Zn symmetric cells at 10 mA cm^{-2}/1 mAh cm^{-2} at room temperature; (E) Galvanostatic cycling of Zn//Zn symmetric cells at 40 °C and 0.5 mA cm^{-2}/0.25 mAh cm^{-2}; (F) Comparison of the cycling durability achieved in this work with previously reported surface-modified zinc electrodes; (G) Coulombic efficiency of Zn//Cu cells at 0.2 mA cm^{-2}/0.1 mAh cm^{-2}; (H) Coulombic efficiency of Zn//Cu cells at 1 mA cm^{-2}/0.5 mAh cm^{-2}. CE: Coulombic efficiency; ZP: zinc powder; CB: carbon black; rGO: reduced graphene oxide; CNT: carbon nanotube; MXene: two-dimensional transition-metal carbides, nitrides, and carbonitrides. Mxene

monitor the time-dependent interfacial kinetics during Zn plating/stripping [Figure 3D and E]. The short-, intermediate-, and long-relaxation-time regions [$\log_{10}(\tau/s) \approx$ -5 to -3, -3 to -1, and -1 to 1] are qualitatively associated with fast interfacial/surface-film processes, charge-transfer processes, and slower ion-transport/concentration-polarization processes, respectively. During plating, pristine ZP shows progressively intensified intermediate- and long-time responses, followed by a broad increase after polarity reversal at ~3,600 s, whereas ZP@CuC_2O_4 shows weaker, more localized DRT features, indicating reduced impedance accumulation and more stable interfacial kinetics during repeated plating/stripping.

To corroborate the electrochemical findings, SEM and EDS mapping were employed to visualize the morphological evolution and elemental distribution of the electrodes. Prior to cycling, SEM images and

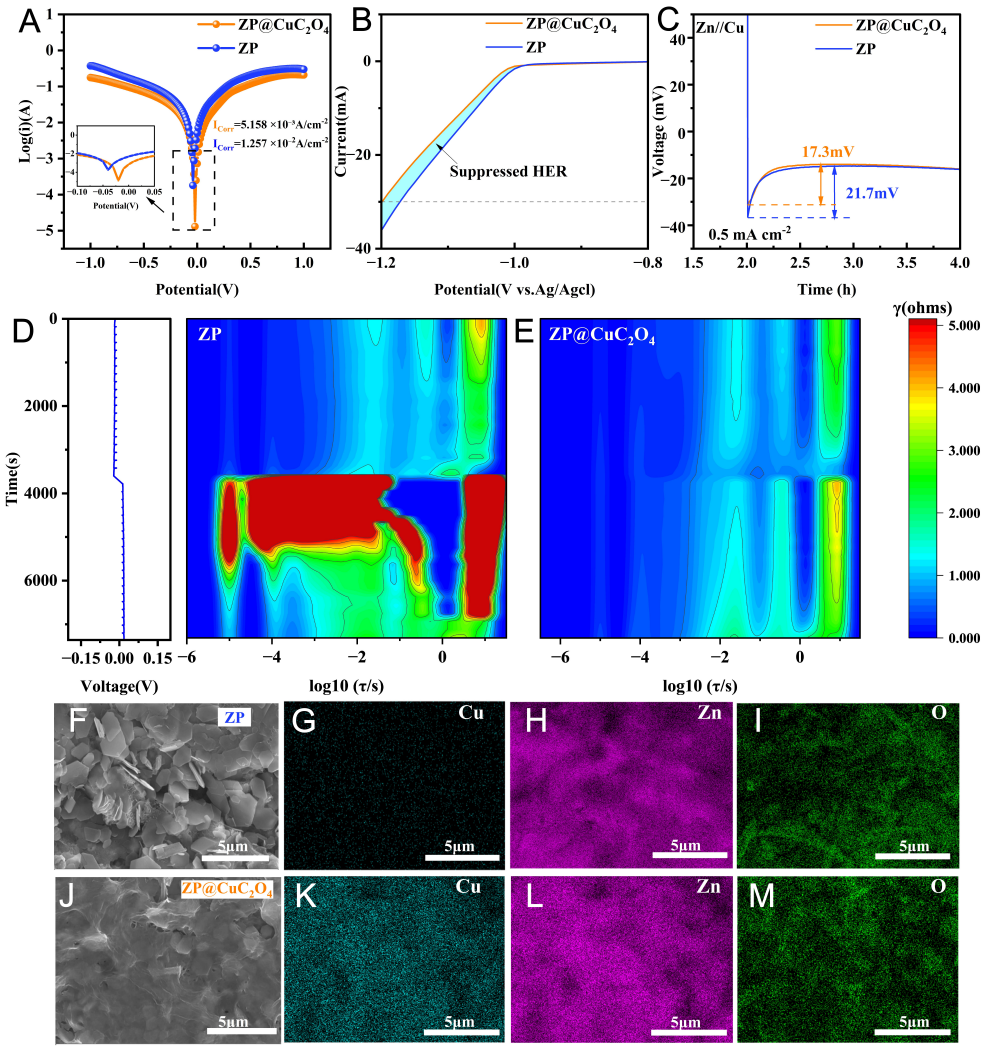


Figure 3. Interfacial kinetics and deposition morphology of ZP and ZP@CuC_2O_4 electrodes. (A) Tafel plots of ZP and ZP@CuC_2O_4; (B) Linear sweep voltammetry curves of ZP and ZP@CuC_2O_4 electrodes; (C) Overpotential comparison of ZP and ZP@CuC_2O_4 electrodes in Zn//Cu cells at 0.5 mA cm^{-2}; (D and E) DRT contour plots derived from in situ electrochemical impedance spectroscopy of Zn//Zn symmetric cells using ZP and ZP@CuC_2O_4 electrodes, respectively; the vertical axis denotes the elapsed electrochemical testing time (s), and the color scale γ(τ) (Ω) represents the impedance contribution at each characteristic relaxation time; (F) SEM image of the ZP electrode after 100 cycles at 1 mA cm^{-2} and (G-I) corresponding EDS maps; (J) SEM image of the ZP@CuC_2O_4 electrode after 100 cycles at 1 mA cm^{-2} and (K-M) corresponding EDS maps. SEM: Scanning electron microscope; EDS: energy-dispersive X-ray spectroscopy; HER: hydrogen evolution reaction; ZP: zinc powder; DRT: distribution of relaxation times.

corresponding EDS mapping confirm the homogeneous incorporation of Cu-containing species within the ZP@CuC_2O_4 architecture [Supplementary Figures 7 and 8, Supplementary Materials], establishing a uniform initial interface. Following 100 cycles at a current density of 1 mA cm^{-2}, the unmodified ZP electrode exhibits severe morphological degradation. The surface is characterized by rough, loose accumulations and distinct localized protrusions [Figure 3F], indicative of uncontrolled dendritic growth and uneven zinc deposition. Concurrently, elemental mapping reveals a complete absence of copper signals [Figure 3G-I], confirming the lack of a protective modulator layer. In stark contrast, the cycled ZP@CuC_2O_4 electrode maintains a planar, compact, and dendrite-free morphology [Figure 3J]. The corresponding elemental maps [Figure 3K-M] display a highly uniform distribution of Cu, O, and Zn across the electrode surface. This persistent uniformity suggests that the CuC_2O_4 modification possesses robust structural integrity, rather than detaching or deactivating during prolonged cycling. The interfacial layer continues to effectively regulate ion flux and guide the homogeneous expansion of the reaction zone, thereby preventing the formation of "dead zinc" and

ensuring stable plating/stripping behavior. Cross-sectional SEM further shows a more heterogeneous and discontinuous through-thickness morphology for the cycled ZP electrode, whereas ZP@CuC_2O_4 retains a comparatively more continuous and uniform internal structure [Supplementary Figure 9, Supplementary Materials]. Such suppression of localized Zn growth is consistent with previous interfacial-regulation studies demonstrating that homogenized interfacial Zn^{2+} transport and deposition can mitigate dendritic growth and parasitic reactions[36]. To further evaluate the morphological stability of the Zn anode under elevated-temperature conditions, post-cycling SEM and EDS characterizations were performed on electrodes retrieved from Zn//Zn symmetric cells cycled at 40 °C. Compared with pristine ZP, ZP@CuC_2O_4 retains a more compact, uniform surface morphology and a more homogeneous elemental distribution after high-temperature cycling [Supplementary Figure 10, Supplementary Materials].

To elucidate how CuC_2O_4 regulates the zinc anode interface during operation, multimodal spectroscopic characterizations were performed on ZP@CuC_2O_4 before and after discharge. The structural origin of the introduced modifier was first verified using CuC_2O_4 powder. Its XRD pattern matches the reported CuC_2O_4 phase well, with a characteristic (110) reflection near 22.7°, confirming the crystallographic identity of the modifier [Supplementary Figure 11, Supplementary Materials][37]. Raman spectroscopy also shows characteristic vibrational features associated with coordinated oxalate species, indicating that the initial CuC_2O_4 phase contains a distinct carbonyl-dominated coordination environment [Supplementary Figure 12, Supplementary Materials][38]. After discharge to -1.2 V, however, the characteristic (110) diffraction peak of CuC_2O_4 disappeared [Figure 4A], indicating that the original crystal structure had been disrupted. This structural evolution was further corroborated by vibrational spectroscopy. In the FT-IR spectrum, the ν(C=O) vibration was markedly weakened, whereas the ν(C-O) vibration was significantly enhanced, accompanied by an intensified ν(-OH) signal [Figure 4B]. It should be noted that the ν(-OH) band is not sufficiently specific for an unambiguous structural assignment and may also contain contributions from adsorbed/interfacial water, residual electrolyte, and hydroxide- or basic zinc salt-related species formed during cycling. Therefore, the ν(-OH) variation is considered only as auxiliary evidence, while the proposed reconstruction is primarily supported by the coordinated changes in the C=O/C-O features together with the XRD and XPS results. Raman results likewise show that the characteristic C=O peak near 1,520 cm^{-1} became markedly weaker after discharge [Figure 4C]. These results consistently indicate that CuC_2O_4 did not remain structurally unchanged during discharge, but instead underwent a discharge-triggered phase transition, in which the original Cu(II)-oxalate framework evolved from a C=O-dominated state toward a more C-O-enriched configuration.

XPS results provide more direct chemical evidence for this phase transition. In the O 1s spectrum, the pristine electrode surface was primarily characterized by Zn-O species from the native oxide layer, together with distinct C=O and C-O components arising from the oxalate coordination structure of CuC_2O_4. After discharge, the Zn-O peak was markedly weakened, whereas the C-O-related component was significantly enhanced, indicating that the interfacial oxygen environment shifted from an initial Zn-O/C=O-rich state toward a more C-O-enriched configuration [Figure 4D]. Consistently, the O-C=O signal in the C 1s spectrum decreased, while the C-O component increased simultaneously [Figure 4E], suggesting that the original Cu-oxalate coordination environment was partially transformed from a carbonyl-dominated state into a more C-O-enriched single-bond configuration during discharge[28]. Further evidence was provided by the Cu 2p spectrum. Cu in the pristine electrode mainly existed as Cu^{2+}, whereas after discharge the main peaks shifted to lower binding energies and the satellite peaks largely disappeared, indicating the formation of Cu^{+}-related species [Figure 4F][28]. A plausible explanation is that cathodic electron injection destabilized the Cu(II)-oxalate framework in the hydrated interfacial environment, thereby inducing reduction of the Cu center together with reorganization of oxalate ligand bonding[28,29,39]. These results collectively demonstrate the first key mechanistic feature: the discharge-triggered phase transition of CuC_2O_4 itself. While the present

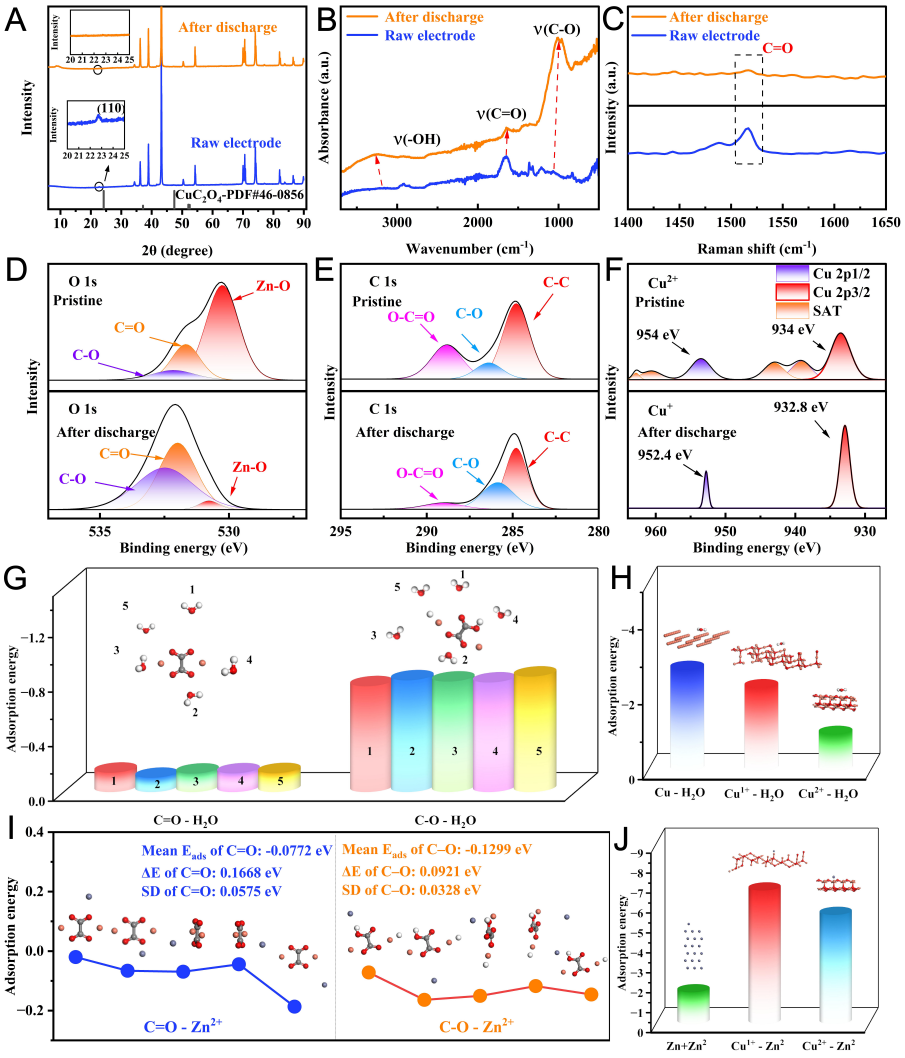


Figure 4. Structural evolution and theoretical analysis of the CuC_2O_4-modified interface. (A) XRD patterns, (B) FT-IR spectra, (C) Raman spectra, (D-F) XPS O 1s, C 1s, and Cu 2p spectra of ZP@CuC_2O_4 before and after discharge; (G) DFT-calculated H_2O adsorption energies at C=O and C-O sites; (H) DFT-calculated H_2O adsorption energies at Cu, Cu^+, and Cu^{2+} sites; (I) DFT-calculated Zn^{2+} adsorption energies at C=O and C-O sites; (J) DFT-calculated Zn^{2+} adsorption energies at Zn, Cu^+, and Cu^{2+} sites. XRD: X-ray diffraction; FT-IR: Fourier-transform infrared; XPS: X-ray photoelectron spectroscopy; DFT: density functional theory; SD: standard deviation; ΔE: energy spread; PDF: powder diffraction file.

characterization primarily captures the structural and chemical states before and after discharge, future operando spectroscopic studies could provide further insight into the temporal evolution and reversibility of the interfacial reconstruction. Complementary *in-situ* electrochemical techniques, such as scanning electrochemical microscopy (SECM), may further provide spatially resolved information on local interfacial electrochemical activity[40]. A schematic summary of the proposed structural evolution is provided in Supplementary Figure 13 [Supplementary Materials]. The Cu(II)-to-Cu(I) reduction associated with this reconstruction is a Faradaic process with a finite charge contribution. Complete one-electron reduction corresponds to a theoretical capacity of approximately 176.8 mAh g^{-1} of CuC_2O_4, equivalent to an upper-bound contribution of ~3.54 mAh g^{-1} for the electrode containing 2 wt% CuC_2O_4. This finite reconstruction-related charge is therefore distinct from continuously accumulating parasitic charge consumption associated with hydrogen evolution and corrosion. Within the scope of the present evidence, the resulting C-O-enriched and Cu(I)-related interfacial environment is considered to be largely retained during subsequent cycling rather than undergoing a complete Cu(II)/Cu(I) and C=O/C-O reversal in each plating/stripping cycle.

After this phase transition, the newly generated C-O-enriched and Cu^{+}-related surface no longer merely represents a changed copper oxalate structure, but instead functions as a reconstructed interfacial coordination environment for subsequent H_2O and Zn^{2+} regulation. To clarify this second mechanistic component, density functional theory (DFT) calculations were performed to evaluate the adsorption behavior of H_2O and Zn^{2+} at different coordination sites. Here, Zn^{2+} represents the desolvated ionic species after removal of its explicit hydration shell, rather than a hydrated $[Zn(H_2O)_x]^{2+}$ complex. For H_2O adsorption, the calculated adsorption energies at the five representative sites were generally more negative on the C-O sites than on the C=O sites, indicating stronger interactions with H_2O molecules on the post-transition C-O-enriched interface [Figure 4G]. Calculations for the copper sites further indicate that Cu^{+} exhibits stronger interactions with H_2O than Cu^{2+} [Figure 4H], suggesting that the reconstructed interface is more capable of constraining interfacial water molecules. A similar trend was observed for Zn^{2+} adsorption. The average adsorption energy of Zn^{2+} at single-bond oxygen sites (C-O) is -0.1299 eV, which is lower than the -0.0772 eV obtained at carbonyl oxygen sites (C=O), indicating stronger Zn^{2+} binding on the C-O-rich interface [Figure 4I]. Meanwhile, the fluctuation range and standard deviation of the adsorption energies on the C-O sites are both smaller than those on the C=O sites, indicating that Zn^{2+} adsorption in the C-O environment is not only stronger, but also more spatially uniform. In addition, adsorption calculations for different metal centers show that the Cu^{+} site exhibits the strongest binding to Zn^{2+}, significantly outperforming the Cu^{2+} site and the Zn substrate [Figure 4J]. It should be emphasized that these adsorption energies describe the affinity of ionic Zn^{2+} toward the reconstructed interface prior to electrochemical reduction and therefore should not be interpreted as the binding energy of metallic Zn or as the kinetic barrier for subsequent Zn stripping. Thus, the enhanced Zn^{2+} affinity primarily facilitates more favorable and homogeneous Zn^{2+} adsorption and nucleation during plating, but does not necessarily imply inhibited removal of metallic Zn during stripping. These results indicate that the phase transition of CuC_2O_4 further induces an interfacial coordination reconstruction that modulates the interaction with H_2O and Zn^{2+}. The reconstructed interface exhibits stronger water-confinement capability and higher zinc-affinity compared to the pristine surface. This coordination environment promotes more uniform Zn^{2+} adsorption and desolvation, contributing to the enhanced electrochemical stability of the zinc powder anode. It should be noted that the H_2O and Zn^{2+} adsorption energies were calculated independently and therefore should not be directly compared to infer competitive occupation of the same Cu^{+} site. The simultaneous enhancement of water confinement and zinc affinity does not indicate indiscriminate adsorption. Instead, the C-O-enriched environment can immobilize interfacial water through hydrogen-bonding/coordination interactions, thereby reducing the activity of free water toward parasitic reduction, while the Cu^{+}-related sites and oxygen-rich coordination environment provide more uniform Zn^{2+} adsorption sites. This dual regulation suppresses competitive water reduction while guiding homogeneous Zn deposition.

To further evaluate the practical applicability of ZP@CuC_2O_4, we assembled Zn//V_2O_5 full cells to assess its potential for real-world applications. The cyclic voltammetry curves show that the voltage gap decreases from 0.236 V for the ZP cell to 0.198 V for the ZP@CuC_2O_4 cell [Figure 5A], indicating accelerated Zn^{2+}/V^{5+} redox kinetics and reduced polarization. The modified full cell also delivers superior rate capability over 1-10 A g^{-1} [Figure 5B]. During long-term cycling, it retains 82 mAh g^{-1} after 2,000 cycles at 5 A g^{-1} [Figure 5C], while the pristine ZP cell undergoes rapid capacity decay within 520 cycles. At 7 A g^{-1}, the ZP@CuC_2O_4-based full cell also maintains stable capacity output with a coulombic efficiency close to 90%, whereas the bare ZP system fails much earlier [Supplementary Figure 14, Supplementary Materials]. Even at 10 A g^{-1}, a reversible capacity of 78 mAh g^{-1} is retained after 3,600 cycles, far beyond the 1,100-cycle lifetime of the control [Figure 5D]. The advantage remains evident at 15 A g^{-1} as well [Supplementary Figure 15, Supplementary Materials]. Post-cycling SEM and elemental mapping further show that the modified anode preserves a dense and uniform surface after prolonged operation [Figure 5E, Supplementary Figure 16 and Supplementary Table 2, Supplementary Materials], consistent with the enhanced interfacial stability inferred

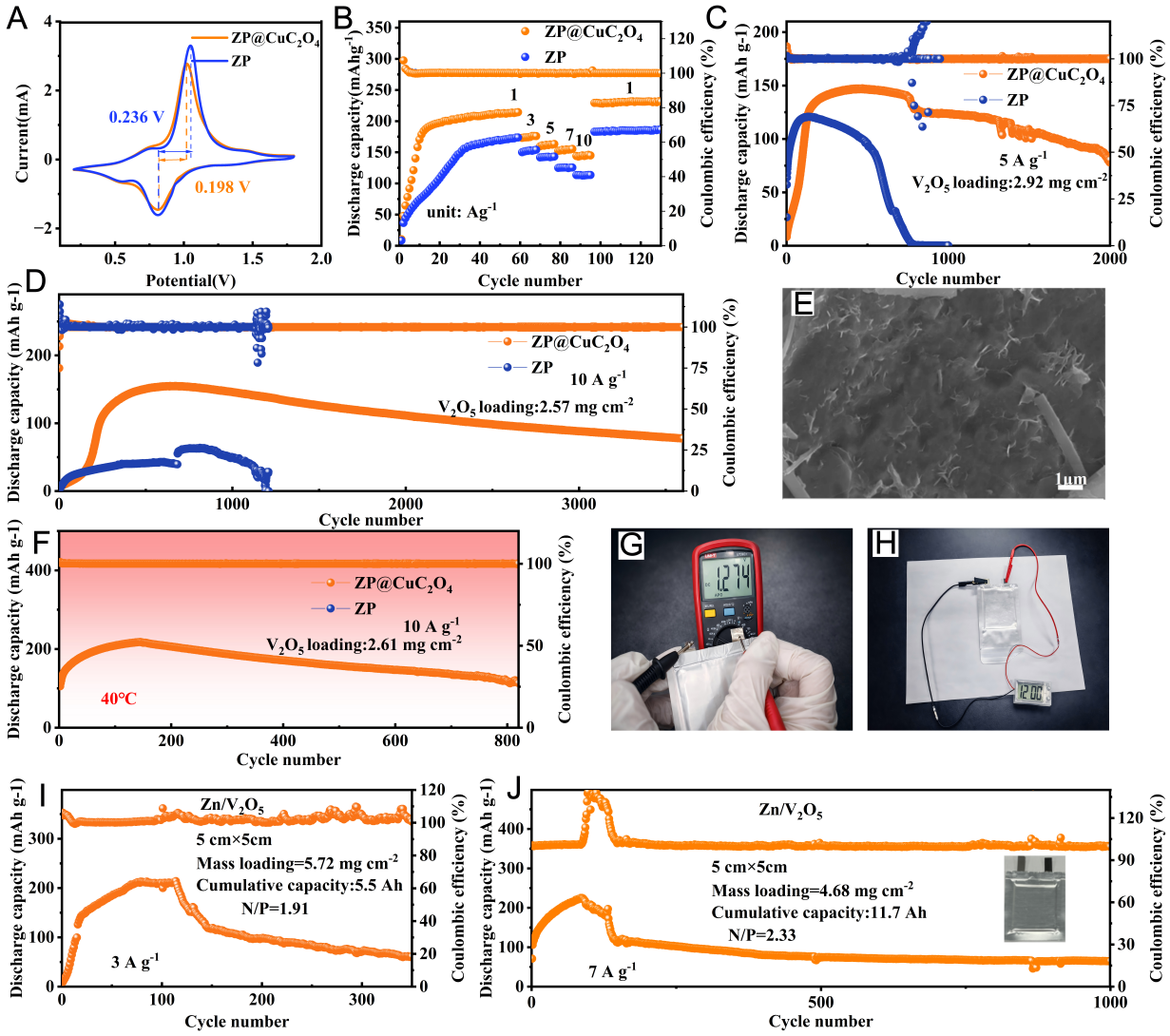


Figure 5. Full-cell and pouch-cell performance of ZP and ZP@CuC_2O_4 electrodes. (A) Cyclic voltammetry curves of Zn//V_2O_5 full cells at 0.1 mV s^{-1}; (B) Rate performance from 1 to 10 A g^{-1}; (C) Long-term cycling performance at 5 A g^{-1}; (D) Long-term cycling performance at 10 A g^{-1}; (E) SEM image of the ZP@CuC_2O_4 electrode after 100 cycles of full-cell cycling; (F) Cycling stability and coulombic efficiency at 40 °C and 10 A g^{-1}; (G) Photograph of the pouch cell at open-circuit voltage, taken by the authors; (H) Photograph of a digital watch powered by a ZP@CuC_2O_4-based pouch cell, taken by the authors; (I) Cycling performance of a pouch cell with a cathode loading of 5.72 mg cm^{-2} at 3 A g^{-1}; (J) Cycling performance of a pouch cell with a cathode loading of 4.68 mg cm^{-2} at 7 A g^{-1}, photograph taken by the authors. SEM: Scanning electron microscope; ZP: zinc powder.

from preceding results.

The robustness of the reconstructed interface is also maintained under elevated temperature and practical device configurations. Elevated temperature generally intensifies water-related parasitic reactions and interfacial instability of zinc anodes[41,42]. At 40 °C, the ZP@CuC_2O_4 full cell still exhibits stable cycling at different current densities, whereas the control cell cannot sustain normal operation [Figure 5F, Supplementary Figures 17-19, Supplementary Materials]. This indicates that the restructured interface induced by CuC_2O_4 not only buffers local polarization and side reactions at room temperature but also effectively suppresses interfacial instability caused by accelerated reactions under high-temperature conditions. To further verify scalability, a 5 cm × 5 cm pouch cell was assembled using the ZP@CuC_2O_4 electrode. The device shows an open-circuit voltage of 1.274 V [Figure 5G] and can directly power a digital

watch [Figure 5H], demonstrating clear output capability. Under a cathode loading of 5.72 mg cm^{-2}, the pouch cell operates stably for 350 cycles at 3 A g^{-1}, with a cumulative discharge capacity of 5.5 Ah [Figure 5I]. Under a cathode loading of 4.68 mg cm^{-2}, it sustains excellent cycling for 1,000 cycles at 7 A g^{-1}, reaches a peak discharge capacity of 225 mAh g^{-1}, and delivers a cumulative capacity of 11.7 Ah [Figure 5J]. The key practical parameters of the pouch cells, including negative-to-positive electrode capacity (N/P) ratio, Zn-anode depth of discharge (DOD), electrolyte volume-to-capacity (E/C) ratio, initial discharge capacity, and capacity retention, are summarized in Supplementary Table 3 [Supplementary Materials]. The transient apparent CE above 100% during the initial cycles of the pouch cell is likely associated with a non-steady-state activation process, during which progressive electrolyte wetting and cathode/interfacial activation cause the accessible discharge capacity to increase more rapidly than the corresponding charge capacity. As the ion-transport pathways and electrode contacts gradually stabilized, the coulombic efficiency rapidly recovered and remained close to 100%, indicating that the cell subsequently entered a stable cycling regime. These results collectively confirm the strong high-rate adaptability, thermal tolerance, and practical application potential of the ZP@CuC_2O_4 anode. To further evaluate the compatibility of the modified Zn anode beyond the V_2O_5 cathode chemistry, ZP@CuC_2O_4 was coupled with an I_2 cathode, and the resulting Zn//I_2 full cells exhibited reversible cycling at 2 and 5 A g^{-1} [Supplementary Figure 20, Supplementary Materials].

CONCLUSIONS

This study demonstrates a phase transformation-driven interfacial coordination reconstruction strategy to mitigate the thermodynamic instability of zinc powder anodes in aqueous zinc-ion batteries. The transformation, characterized by the evolution of the carbon-oxygen framework and copper valence states, facilitates the formation of a robust interphase rich in C-O coordination and Cu^+-related active sites. This dynamically evolved interface effectively regulates Zn^{2+} flux and deposition kinetics, thereby mitigating side reactions and "dead zinc" formation. The ZP@CuC_2O_4 anode demonstrates superior cycling stability under high-rate conditions and maintains high capacity in full cells across a range of temperatures. The strategy of achieving "active regulation" through internal chemical reconstruction provides an alternative approach for stabilizing zinc powder anodes, addressing a key barrier toward practical aqueous zinc-ion batteries.

DECLARATIONS

Authors' contributions

Conceptualization, methodology: Huang, C.; Cao, P.
Software: Li, Y.; Liu, X.
Investigation: Huang, C.; Yang, X.; Yao, S.; Zhu, H.; Yang, J.; Li, C.
Electrochemical experiments and characterization, data curation and analysis, visualization, writing - original draft preparation: Huang, C.
Writing - review and editing: Cao, P.; Lu, Z.
Supervision, project administration: Cao, P.
Resources: Cao, P.; Li, C.
All authors have read and agreed to the published version of the manuscript.

Availability of data and materials

The data supporting the findings of this study are available within the article and its Supplementary Materials. Further data are available from the corresponding author upon reasonable request.

AI and AI-assisted tools statement

During the preparation of this manuscript, the AI tool ChatGPT (version GPT-5.6 Sol, released 2026-07-09) was used for language editing. In addition, the ChatGPT image-generation feature (version GPT-Image2, released 2026-04-21) was used to assist in generating and refining certain schematic visual elements in the Graphical Abstract and Figure 1. All AI-assisted outputs were carefully reviewed, revised, and verified by the authors. These tools did not influence the study design, data collection, analysis, interpretation, or the scientific content of the work. All authors take full responsibility for the accuracy, integrity, and final content

of the manuscript.

Financial support and sponsorship

This work was supported by the National Natural Science Foundation of China (No. 52501268), the Science and Technology Innovation Program of Hunan Province (No. 2025RC3154), the Joint Funds of the Hunan Provincial Natural Science Foundation (Nos. 2025JJ70625 and 2025JJ70666), and the Changsha Municipal Natural Science Foundation (No. kq2502036). The funding agencies had no role in the design of the study, collection, analysis, and interpretation of data, or writing of the manuscript.

Conflicts of interest

All authors declared that there are no conflicts of interest.

Ethical approval and consent to participate

Not applicable.

Consent for publication

Not applicable.

Copyright

© The Author(s) 2026.

Supplementary Materials

Supplementary Materials

REFERENCES

1. Zampardi, G.; La Mantia, F. Open challenges and good experimental practices in the research field of aqueous Zn-ion batteries. *Nat. Commun.* **2022**, *13*, 687. DOI
2. Xie, C.; Li, Y.; Wang, Q.; Sun, D.; Tang, Y.; Wang, H. Issues and solutions toward zinc anode in aqueous zinc-ion batteries: a mini review. *Carbon. Energy.* **2020**, *2*, 540-60. DOI
3. Yang, J.; Yin, B.; Sun, Y.; et al. Zinc anode for mild aqueous zinc-ion batteries: challenges, strategies, and perspectives. *Nano-Micro. Lett.* **2022**, *14*, 42. DOI
4. Li, C.; Jin, S.; Archer, L. A.; Nazar, L. F. Toward practical aqueous zinc-ion batteries for electrochemical energy storage. *Joule* **2022**, *6*, 1733-8. DOI
5. Li, B.; Zhang, X.; Wang, T.; et al. Interfacial engineering strategy for high-performance Zn metal anodes. *Nano-Micro. Lett.* **2022**, *14*, 6. DOI
6. Wen, Q.; Fu, H.; Cui, R.; et al. Recent advances in interfacial modification of zinc anode for aqueous rechargeable zinc ion batteries. *J. Energy. Chem.* **2023**, *83*, 287-303. DOI
7. Ren, Y.; Meng, F.; Zhang, S.; et al. CNT@MnO_2 composite ink toward a flexible 3D printed micro-zinc-ion battery. *Carbon. Energy.* **2022**, *4*, 446-57. DOI
8. Li, Q.; Li, N.; Zhi, C. Zinc powder anodes for rechargeable aqueous zinc-based batteries. *Nano. Lett.* **2024**, *24*, 4055-63. DOI
9. Yan, L.; Zhai, Q.; Zhang, S.; et al. The burgeoning zinc powder anode for aqueous zinc metal batteries: from electrode preparation to performance enhancement. *Adv. Energy. Mater.* **2024**, *14*, 2401328. DOI
10. Huang, J.; Feng, R.; Wu, J.; Lin, W.; Du, W.; Li, C. C. Structural design strategies of zinc powder anode towards rechargeable zinc-based batteries. *Energy. Storage. Mater.* **2025**, *74*, 103934. DOI
11. Yang, Z.; Zhang, Q.; Li, W.; et al. A Semi-solid zinc powder-based slurry anode for advanced aqueous zinc-ion batteries. *Angew. Chem. Int. Ed.* **2023**, *62*, e202215306. DOI
12. Du, W.; Ang, E. H.; Yang, Y.; Zhang, Y.; Ye, M.; Li, C. C. Challenges in the material and structural design of zinc anode towards high-performance aqueous zinc-ion batteries. *Energy. Environ. Sci.* **2020**, *13*, 3330-60. DOI
13. Zhang, Q.; Luan, J.; Tang, Y.; Ji, X.; Wang, H. Interfacial design of dendrite-free zinc anodes for aqueous zinc-ion batteries. *Angew. Chem. Int. Ed.* **2020**, *59*, 13180-91. DOI
14. Dong, L.; Yang, W.; Yang, W.; et al. Flexible and conductive scaffold-stabilized zinc metal anodes for ultralong-life zinc-ion batteries and zinc-ion hybrid capacitors. *Chem. Eng. J.* **2020**, *384*, 123355. DOI

15. Zhou, M.; Guo, S.; Li, J.; et al. Surface-preferred crystal plane for a stable and reversible zinc anode. *Adv. Mater.* **2021**, *33*, 2100187. DOI
16. Yang, X.; Lu, Y.; Liu, Z.; et al. Facet-governed Zn homoepitaxy *via* lattice potential regulation. *Energy. Environ. Sci.* **2024**, *17*, 5563-75. DOI
17. Guo, S.; Qin, L.; Zhang, T.; et al. Fundamentals and perspectives of electrolyte additives for aqueous zinc-ion batteries. *Energy. Storage. Mater.* **2021**, *34*, 545-62. DOI
18. Wang, F.; Borodin, O.; Gao, T.; et al. Highly reversible zinc metal anode for aqueous batteries. *Nat. Mater.* **2018**, *17*, 543-9. DOI
19. Qiu, H.; Du, X.; Zhao, J.; et al. Zinc anode-compatible in-situ solid electrolyte interphase via cation solvation modulation. *Nat. Commun.* **2019**, *10*, 5374. DOI
20. Luo, J.; Xu, L.; Yang, Y.; et al. Stable zinc anode solid electrolyte interphase via inner Helmholtz plane engineering. *Nat. Commun.* **2024**, *15*, 6471. DOI
21. Liu, B.; Yu, L.; Xiao, Q.; et al. *In situ* construction of a static-dynamic hybrid interface toward stable Zn anodes for aqueous Zn-ion batteries. *Chem. Sci.* **2024**, *15*, 16118-24. DOI
22. Yang, H.; Zhu, K.; Xie, W.; Yang, W. Enhancing zinc anode reversibility through dynamic interface engineering with monolayer hydrophobic carbon dots. *ACS. Nano.* **2025**, *19*, 1433-46. DOI
23. Ma, D.; Li, F.; Ouyang, K.; et al. An electrochemically driven hybrid interphase enabling stable versatile zinc metal electrodes for aqueous zinc batteries. *Nat. Commun.* **2025**, *16*, 4817. DOI
24. Yan, H.; Li, S.; Zhong, J.; Li, B. An electrochemical perspective of aqueous zinc metal anode. *Nano-Micro. Lett.* **2024**, *16*, 15. DOI
25. Fan, C.; Meng, W.; Ye, J. Towards advanced zinc anodes by interfacial modification strategies for efficient aqueous zinc metal batteries. *J. Energy. Chem.* **2024**, *93*, 79-110. DOI
26. Zong, Q.; Li, R.; Wang, J.; Zhang, Q.; Pan, A. Tailoring the whole deposition process from hydrated Zn^{2+} to Zn^{0} for stable and reversible Zn anode. *Angew. Chem. Int. Ed.* **2024**, *63*, e202409957. DOI
27. Wu, G.; Yang, W.; Yang, Y.; Yang, H. Dendrite-free strategies for aqueous zinc-ion batteries: structure, electrolyte, and separator. *J. Electrochem.* **2024**, *30*, 2415003. DOI
28. Song, W.; Zhang, J.; Wen, C.; et al. Synchronous redox reactions in copper oxalate enable high-capacity anode for proton battery. *J. Am. Chem. Soc.* **2024**, *146*, 4762-70. DOI
29. Rückriem, K.; Grotheer, S.; Vieker, H.; et al. Efficient electron-induced removal of oxalate ions and formation of copper nanoparticles from copper(II) oxalate precursor layers. *Beilstein. J. Nanotechnol.* **2016**, *7*, 852-61. DOI
30. Zhang, K.; Cui, D.; Huang, X.; et al. Insights into the interfacial chemistry and conversion mechanism of iron oxalate toward the reduction by lithium. *Chem. Eng. J.* **2021**, *426*, 131446. DOI
31. Zhao, C.; Zhang, Y.; Gao, J.; et al. Zincophilic design and the electrode/electrolyte interface for aqueous zinc-ion batteries: a review. *Batteries. Supercaps.* **2023**, *6*, e202200478. DOI
32. Li, H.; Zhao, R.; Zhou, W.; et al. Trade-off between zincophilicity and zincophobicity: toward stable Zn-based aqueous batteries. *JACS. Au.* **2023**, *3*, 2107-16. DOI
33. Li, C.; Liang, L.; Liu, X.; et al. A lean-zinc anode battery based on metal-organic framework-derived carbon. *Carbon. Energy.* **2023**, *5*, e301. DOI
34. Li, G.; Zhang, S.; Yuwono, J. A.; et al. Hydrophobic liquid electrolyte interphases for efficient aqueous zinc batteries. *Nat. Nanotechnol.* **2026**, *21*, 967-75. DOI
35. Peng, Z.; Li, S.; Tang, L.; Zheng, J.; Tan, L.; Chen, Y. Water-shielding electric double layer and stable interphase engineering for durable aqueous zinc-ion batteries. *Nat. Commun.* **2025**, *16*, 4490. DOI
36. Jeong, D. Y.; Chang, W. J.; Jang, S.; et al. Controlling dendrite growth and side reactions in anode-free Zn-ion aqueous batteries with PMMA:Zn coated electrode. *J. Energy. Storage.* **2024**, *76*, 109791. DOI
37. Christensen, A. N.; Lebech, B.; Andersen, N. H.; Grivel, J. The crystal structure of paramagnetic copper(II) oxalate (CuC_2O_4): formation and thermal decomposition of randomly stacked anisotropic nano-sized crystallites. *Dalton. Trans.* **2014**, *43*, 16754-68. DOI
38. Edwards, H.; Farwell, D.; Rose, S.; Smith, D. Vibrational spectra of copper (II) oxalate dihydrate, $CuC_2O_4{\cdot}2H_2O$, and dipotassium bis-oxalato copper (II) tetrahydrate, $K_2Cu(C_2O_4)_2{\cdot}4H_2O$. *J. Mol. Struct.* **1991**, *249*, 233-43. DOI
39. Angamuthu, R.; Byers, P.; Lutz, M.; Spek, A. L.; Bouwman, E. Electrocatalytic CO_2 conversion to oxalate by a copper complex. *Science* **2010**, *327*, 313-5. DOI
40. Liu, T.; Hua, W.; Yuan, H.; et al. Direct in situ measurement of electrocatalytic carbon dioxide reduction properties using scanning electrochemical microscopy. *J. Anal. Test.* **2025**, *9*, 202-12. DOI
41. Xie, Y.; Dou, Q.; Li, G.; Chen, Y.; Yan, X. Regulating the solvation environment of hybrid electrolytes towards high-temperature zinc-ion storage. *Energy. Mater.* **2025**, *5*, 500025. DOI

42. Xue, T.; Mu, Y.; Wei, X.; et al. From fundamentals to practice: electrolyte strategies for zinc-ion batteries in extreme temperature. *Carbon. Neutralization.* **2025**, *4*, e183. DOI

Disclaimer/Publisher's Note: All statements, opinions, and data contained in this publication are solely those of the individual author(s) and contributor(s) and do not necessarily reflect those of OAE and/or the editor(s). OAE and/or the editor(s) disclaim any responsibility for harm to persons or property resulting from the use of any ideas, methods, instructions, or products mentioned in the content.

© The Author(s) 2026. Open Access This article is licensed under a Creative Commons Attribution 4.0 International License (https://creativecommons.org/licenses/by/4.0/), which permits unrestricted use, sharing, adaptation, distribution and reproduction in any medium or format, for any purpose, even commercially, as long as you give appropriate credit to the original author(s) and the source, provide a link to the Creative Commons license, and indicate if changes were made.